A 2D model for a gliding arc discharge

Reference:

Kolev Stanimir, Bogaerts Annemie.- *A 2D model for a gliding arc discharge*
Plasma sources science and technology / **Institute of Physics** - ISSN 0963-0252 - 24:1(2015), 015025
DOI: http://dx.doi.org/doi:10.1088/0963-0252/24/1/015025

2D model for a gliding arc discharge

St Kolev[1,2], **A Bogaerts**[1]

[1]Research group PLASMANT, Department of Chemistry, University of Antwerp, Universiteitsplein 1, B-2610 Antwerp, Belgium

[2]Faculty of Physics, Sofia University, 5 James Bourchier Boulevard, 1164 Sofia, Bulgaria

E-mail: skolev@phys.uni-sofia.bg

E-mail: annemie.bogaerts@uantwerpen.be

Abstract. In this study we report on a two-dimensional fluid model of a gliding arc discharge in argon. Despite the 3D nature of the discharge, 2D models are found to be capable of providing very useful information about the discharge operation. We employ two models – an axisymmetric and a Cartesian one. We show that for the considered experiment and conditions of a low current arc (around 30 mA) in argon, there is no significant heating of the cathode surface and the discharge is sustained by field electron emission from the cathode accompanied with the formation of a cathode spot. The obtained discharge power and voltage are relatively sensitive to the surface properties and particularly to the surface roughness, causing effectively an amplification of the normal electric field. The arc body and anode region are not influenced by this and depend mainly on the current value. The gliding of the arc is modelled by means of a 2D Cartesian model. The arc-electrode contact points are analysed and the gliding mechanism along the electrode surface is discussed. Following experimental observations, the cathode spot is simulated as jumping from one point to another. A complete arc cycle is modelled - from initial ignition to arc decay. The results show that there is no interaction between the successive gliding arcs.

PACS numbers: 52.50.Dg, 52.50.Nr, 52.65.Kj, 52.80.Mg

Keywords: gliding arc discharge, sliding arc discharge, fluid plasma model, atmospheric pressure plasmas

1. Introduction

Gliding arc discharges (GAD), also called travelling or sliding arc discharges, have been applied successfully for plasma assisted gas processing in chemistry and environmental protection [1, 2]. In general a GAD is a non-stationary arc discharge between two diverging electrodes submerged in a gas flow. The arc is self-initiated at the shortest electrode distance and pushed by a gas flow toward the diverging electrode region. The arc length grows until the applied voltage becomes insufficient to sustain the extended arc length or until another arc is initiated at the shortest electrode distance. The gas flow is usually enforced by an external gas source or it is produced as a result of the gas

heating and the gas convection (Jacob's ladder discharge [3]). The GAD can operate in a relatively wide range of conditions, i.e. a pressure ranging from a few Torr to atmospheric pressure and above, and an arc current from several milliamperes to tens of amperes. This wide range of possible operation conditions means a wide range of plasma/gas parameters and thus it gives flexibility for the use of a GAD in various applications. The arc could also have rather different properties within the different stages of its travel along the electrodes. For currents of several amperes the initial arc is close to local thermal equilibrium (LTE) while the arc close to extinction is far from LTE. At very low current values (100 mA and below) the discharge could have the properties of a glow discharge even at atmospheric pressure [4–7]. The glow-to-arc transition occurs with the rise of the current and the value of this transition depends on the discharge conditions and the gas type. The GAD can be powered by slightly different electrical schemes but all of them are relatively cheap and easy to build, thus being very attractive for industrial application.

In the last 10-20 years there is a growing interest in GADs for plasma chemistry applications [1, 2]. Different configurations have been proposed [1] and a considerable number of experimental studies at different conditions have already been reported (see [1, 8] and the references therein). GADs used for CO_2 reforming are gaining importance in recent years due to their promising energy efficiency [1, 9–11]. In this paper, we present a detailed model of a GAD, to obtain a better insight in its properties and behaviour, in order to improve this application. A good plasma model should give substantial information for the discharge operation and the background chemistry and serve as a tool for further design optimizations.

Building a comprehensive model of a GAD is not a trivial task. There are several reasons for that. First of all, the discharge geometry makes this inherently a 3D problem and the model can not be reduced to 2D without relying on certain assumptions. Another difficulty is the discharge ignition accompanied by positive streamer propagation and transition to arc or glow discharge when the cathode is reached by the streamer. This is a rather fast (less than a microsecond) process and it is very difficult to model due to the extreme electric fields at the streamer head and the gas pre-ionization in front of it due to photoionization. A third difficulty arises from the treatment of the electrode phenomena like the cathode spot and its motion along the electrode. The formation of cathode spots is considered as self-organizing phenomena [12] which are heavily studied [13] and there is an ongoing discussion in the literature about their nature and characteristics [12]. They are the result of a concentrated arc current through a very tiny channel near the cathode with a diameter in the order of 20-200 μm. Usually they are highly non-stationary structures, moving in a quasi-random way and causing melting and sputtering of the cathode surface. The physics of these phenomena is still under active research [12–14]. From the modelling perspective, the description of such tiny moving current channel is very difficult and certain approximations need to be made. Moreover, the large difference in size between the spot (order of 20-200 μm) and the whole arc (order of several cm) requires the use of

an unstructured discretization grid, which should also adapt in time in order to follow the gliding arc motion. In case of low current GAD in glow discharge mode the cathode spot might be wider than the plasma column [4–7] with the corresponding cathode fall region. A fourth complication is that one should also take into account that at least in some stages of the arc evolution, the plasma is not in local thermal equilibrium (LTE) and the electron thermal balance should be considered separately from the heavy species energy balance. Fifth, to make the situation even worse, the plasma description should also be coupled to a gas flow description, which for some experimental set-ups and conditions is more turbulent than laminar. Finally, the arc has a quasi-random highly irregular shape, as is observed in most of the high speed photographs of the discharge, especially at low current conditions. Such behaviour could not be well described by deterministic models like a fluid plasma model, and Monte Carlo-like models should be employed. The latter are however rather expensive from computational point of view.

Probably because of these main reasons, there are not many papers in the literature on GAD modelling [8,9,15–19]. Most of them are based on the relatively simplified well known Elenbaas-Heller equation, assuming an equilibrium plasma. While this certainly is a good approximation for higher current arcs, it is rather questionable for lower current GADs (like the one we consider here) and during the non-equilibrium discharge stage when the arc is long and close to decay. In [16] the treatment is extended to a non-equilibrium plasma based on an analytical relation between the electric field and the electron and gas temperatures. Some of the studies also focus only on the calculation of the discharge electrical parameters [19] or only consider a 0D model in the case of a complex chemistry [9].

Our approach for the GAD modelling is to use a fluid plasma model, considering self-consistently the charged species interaction with the electric field, i.e. solving the species conservation equations together with the Poisson equation. The model is also coupled with the gas flow and gas temperature description, as well as with the cathode heat balance for properly taking into account the electron emission processes. Obviously, solving all these equations in 3D for a complex gas like CO_2 is a challenging task even for modern computers. Instead of directly building such a model, we intend to study the GAD by gradually increasing the model complexity. This strategy has several advantages, but mainly it allows us to address different questions with the most suitable models (in a relatively fast way). For example there is no point of studying the general discharge behaviour using a complex gas like CO_2, we could do that very well with a much simpler gas and obtain reliable results much faster. We will describe in details our model in section 2.

In this paper, after presenting our model and the strategies we consider for the GAD modelling, we analyse the general discharge behaviour and the influence of the cathode material properties and particularly the electron emission processes on the results for the arc parameters. For this purpose, we use in first instance a 2D axisymmetric model considering a steady non-gliding arc in argon. Furthermore, we also discuss the arc gliding mechanism by means of a 2D Cartesian model again in argon. In the near future

we intend to extend our 2D model to 3D, and compare with experimental measurements. Later we will focus on a GAD model in CO_2 and the discharge application for CO_2 reforming.

The paper has the following structure: In section 2 we describe in detail the model developed for the GAD description - reaction set, equations and boundary conditions. The results are presented and discussed in section 3, including an analysis of the cathode heating in section 3.1, the influence of the cathode surface properties on the electron emission in section 3.2, analysis of the arc contact points with the electrodes in section 3.3, and demonstration of the arc gliding along the electrodes in section 3.4.

2. Model description

2.1. Simplifications of the model

The complexity of the gliding arc discharge determines the need of certain simplifications in the model in order to obtain a solution within a reasonable time span with current computing resources. Below we explain the most important simplifications in our model: 1) The first approximation is to use a fluid plasma model for the description of a phenomenon which clearly has a semi-stochastic behaviour. Thus here we will describe some kind of averaged (representative) gliding arc. To do that, we will rely quite often on experimental data for defining effective plasma/arc parameters, like arc velocity, arc length, etc. 2) The streamer stage in the arc ignition will be completely omitted. Instead the arc will be artificially ignited by creating a plasma channel in the very beginning of the gliding arc simulation. Indeed, the real arc ignition is a very short process and in practice it does not influence the arc plasma characteristics. 3) The gas velocity is calculated initially without taking into account the gas heating due to the discharge and the calculated velocity is used as input data for the rest of the model. 4) The ion temperature is assumed to be equal to the gas temperature, which is reasonable for atmospheric pressure discharges. Numerical tests show that the ion temperature differs significantly (20-30%) only within the cathode fall, where their motion is determined by the strong electric field. Within the arc body the ion temperature exceeds the gas temperature with less than 15%. 5) The cathode spot motion along the cathode is controlled externally by following the anode arc contact point.

2.2. Geometries considered in the model

Despite the considerable number of (reasonable) approximations, the model developed here is still quite elaborate and it couples a self-consistent plasma-field description with the gas flow, gas and electrode heating and current distribution at the cathode. In this work we present results from two 2D models – an axisymmetric model describing a steady arc and a Cartesian model demonstrating the gliding of a "2D arc", which is basically an infinite plasma slab. In reality, the gliding arc problem is a 3D problem and we can only compare quantitatively the results from a 3D model with experiments. However, the 3D

model takes months to compute and requires significant computer resources. Therefore, before going into brute force calculations of the 3D model, we need to verify and test the whole model in 2D. Although the 2D models could provide only approximate results, they are still able to give us very useful qualitative and quantitative information on the discharge physics, and moreover they demonstrate very well the employed modelling strategies.

The gliding arc models developed here include numerous coupled partial differential equations (PDEs) solved with the commercial software COMSOL Multiphysics ®(version 4.3a). The software allows a relatively large number of equations to be coupled relatively easily and it comes with sophisticated meshing capabilities. The latter is crucial for the GAD modelling. The plasma model is based on the Plasma Module within COMSOL. In order to be able to verify our results, we model a particular experiment and compare with measured discharge characteristics. Here we consider the geometry and conditions of the experiments published in [20, 21], which were also performed in pure argon. The experimental set-up is described in detail in [20] and several important discharge characteristics are measured – electron density, gas temperature, current and voltage signals, as well as fast imaging of the gliding arc. This provides enough input data for our models, like current and voltage signals, and at the same time additional data for verification of the model results, like electron density and gas temperature. As mentioned above, in this work we use two 2D models, considering axisymmetric and Cartesian geometry. Both models are based on the same argon kinetics and similar but a slightly different set of equations, depending on the model specific aim.

The aim of the 2D axisymmetric model is to provide results for a steady non-gliding arc which we expect to resemble the characteristics of a real gliding arc, but only in the very beginning of the arc evolution and ignoring the convective cooling, i.e. immediately after breakdown at the smallest electrode distance when the arc is only slightly bent by the gas flow. We should stress, however, that the convective cooling at that stage will have a considerable influence on the arc parameters and probably it will cause an enhancement of the arc contraction. Despite these limitations, the model proves to be very useful. It allows us to study the cathode heating and its importance for the arc parameters. As we will show later in subsection 3.1, there is no significant cathode heating for the considered conditions and thus we can safely assume a cold cathode. The axisymmetric model is also an excellent test set-up for the study of the results sensitivity with respect to external parameters which are not well known, like the field enhancement factor (FEF) and the secondary electron emission coefficient. This will be commented in detail in subsection 3.2. The model considers a discharge between two circular plates with 3.2 mm distance between them. The distance corresponds to the shortest distance between the electrodes in the experiments of [20, 21]. The geometry is schematically shown in figure 1(a). The figure represents the correct aspect ratio of the simulated geometry. The domain (and cathode) radius is 50 mm and the cathode thickness is 20 mm.

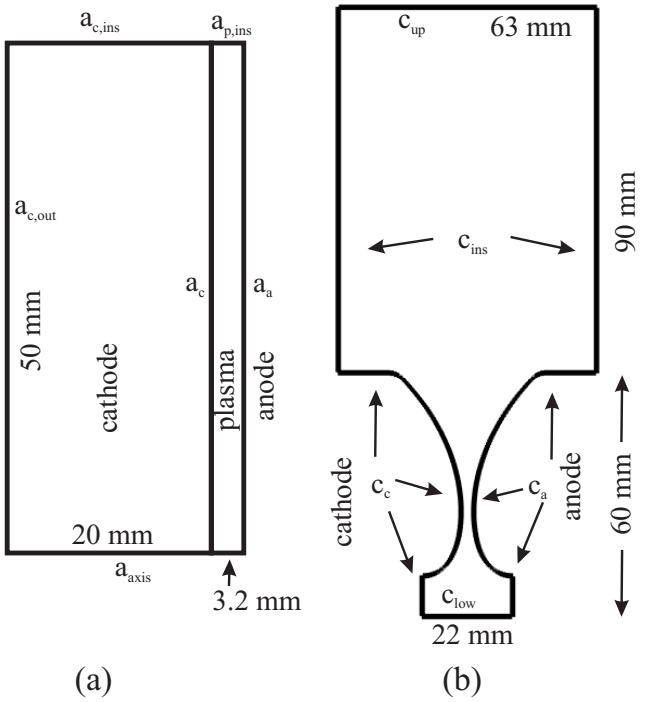

Figure 1. Geometries considered in the models:

(a) 2D axisymmetric model geometry with the following boundaries: a_c - cathode-plasma interface, a_a - anode, a_{axis} - axial symmetry axis, $a_{c,out}$ - cathode-outer environment interface (room temperature), $a_{c,ins}$ - insulation boundary, $a_{p,ins}$ - insulation boundary for the plasma (zero fluxes).

(b) 2D Cartesian model geometry with the following boundaries: c_c - cathode, c_a - anode, c_{low} - upstream boundary used as a gas inlet, c_{ins} - insulated (symmetry) boundaries imposing zero normal fluxes, c_{up} - upper (downstream) boundary providing gas outflow.

The 2D Cartesian model aims at demonstrating the arc gliding process and qualitatively studying some phenomena specific for the gliding arc, like gliding of the arc contact points along the electrodes, interaction between consecutive arcs, arc cooling due to arc extension as a result of the gas flow, etc. The model considers the exact shape and size of the electrodes used in the experiments [20], but it considers them as infinite in the transverse (z) direction (figure 1(b)). Therefore, the arc established in this model does not have a circular cross section as it is in the real experiment, but it is an infinite slab. Despite the non-realistic arc geometry produced here, this model is very useful for studying the different methods of the arc gliding along the electrode surface and it gives valuable results for the discharge operation. The schematic picture in figure 1(b) has the real aspect ratio of the geometry considered in the model. The minimum distance between the electrodes is 3.2 mm, the height of the domain above the electrodes is 90 mm, while its width (boundary c_{up}) is 63 mm. The height of the curved part of the electrodes is 60 mm.

Table 1. Electron collisions included in the model.

Reaction	Rate coefficient	Reference
(R1) $e + Ar \rightarrow e + Ar$	BS[a]	[22]
(R2) $e + Ar \rightarrow e + Ar(4s)$	BS	[22]
(R3) $e + Ar \rightarrow e + Ar(4p)$	BS	[22]
(R4)[b] $e + Ar \rightarrow e + Ar(4d)$	BS	[22]
(R5) $e + Ar \rightarrow 2e + Ar^+$	BS	[22]
(R6) $e + Ar(4s) \rightarrow e + Ar(4p)$	BS	[23]
(R7) $e + Ar(4s) \rightarrow 2e + Ar^+$	BS	[24]
(R8) $e + Ar(4p) \rightarrow 2e + Ar^+$	BS	[24]
(R9) $e + Ar(4s) \rightarrow e + Ar$	BS, DB[c]	[22]
(R10) $e + Ar(4p) \rightarrow e + Ar$	BS, DB	[22]
(R11) $e + Ar(4p) \rightarrow e + Ar(4s)$	BS, DB	[23]
(R12) $Ar^+ + 2e \rightarrow Ar + e$	$k_{(m^6/s)} = 8.75 \times 10^{-39} T_e^{-4.5}(eV)$	[25]
(R13) $Ar^+ + e + Ar \rightarrow Ar + Ar$	$k_{(m^6/s)} = 1.5 \times 10^{-40} (T_g(K)/300)^{-2.5}$	[26]
(R14) $Ar_2^+ + e \rightarrow Ar^+ + Ar + e$	$k_{(m^3/s)} = 1.11 \times 10^{-12} \exp\left(-\frac{2.94-3(Tg(eV)-0.026)}{Te(eV)}\right)$	[27]
(R15) $Ar_2^+ + e \rightarrow Ar + Ar(4s)$	$k_{(m^3/s)} = 1.04 \times 10^{-12} [300/T_e(K)]^{0.67} \frac{1-\exp[-418/Tg(K)]}{1-0.31\exp[-418/Tg(K)]}$	[28, 29]
(R16) $Ar_2^* + e \rightarrow Ar_2^+ + 2e$	$k_{(m^3/s)} = 9 \times 10^{-14} [T_e(eV)]^{0.7} \exp[-3.66/T_e(eV)]$	[30]
(R17) $Ar_2^* + e \rightarrow 2Ar + e$	$k_{(m^3/s)} = 1 \times 10^{-15}$	[30]

[a] Boltzmann solver: The rate coefficients are calculated from the corresponding cross sections, based on solution of the Boltzmann equation with BOLSIG+ [31]

[b] This process is included only as an energy loss channel without considering the conservation equation for Ar(4d)

[c] Detailed balance: The rate coefficients for the superelastic processes are calculated using the detailed balance principle [32] incorporated in BOLSIG+ [31].

2.3. Argon kinetics

The argon kinetics taken into account is not very detailed and one can find in the literature much more elaborative argon kinetics. However, the complexity of the discharge itself requires significant computational resources and therefore the chemical kinetics should be limited to a reasonable extent if we aim at reasonable computation times. The model considers the following species: e – electrons, Ar – Argon atoms, Ar^+ – Argon ions, Ar_2^+ – Argon molecular ions, Ar (4s) – all 4s levels considered as a single lumped excitation level, Ar (4p) – all 4p levels considered as a single lumped excitation level, and Ar_2^* – which includes $Ar_2(^1\Sigma_u^+)$ and $Ar_2(^3\Sigma_u^+)$ excited molecules. The different processes considered in both models are listed in tables 1 and 2, along with the corresponding references for the rate coefficients and cross sections.

2.4. System of equations

The two models consider a slightly different set of equations, which is related to their specific aim and geometry. The 2D axisymmetric model considers the particle balance equations, the electron energy balance equation, the gas and cathode thermal balances and the current conservation at the cathode. The 2D Cartesian model, on the other

Table 2. Heavy species collisions and radiative transitions included in the model.

Reaction	Rate coefficient/collision frequency	Reference
(R18) $Ar(4s) + Ar(4s) \rightarrow Ar_2^+ + e$	$k_{(m^3/s)} = \frac{1}{2}6.3 \times 10^{-16}(T_g(K)/300)^{-1/2}$	[33]
(R19) $Ar(4s) + Ar(4s) \rightarrow Ar^+ + Ar + e$	$k_{(m^3/s)} = 1.62 \times 10^{-16}(T_g(K))^{1/2}$	[34]
(R20) $Ar(4s) + Ar(4p) \rightarrow Ar^+ + Ar + e$	$k_{(m^3/s)} = 1.62 \times 10^{-16}(T_g(K))^{1/2}$	[34]
(R21) $Ar(4p) + Ar(4p) \rightarrow Ar^+ + Ar + e$	$k_{(m^3/s)} = 1.62 \times 10^{-16}(T_g(K))^{1/2}$	[34]
(R22) $Ar(4p) + Ar \rightarrow Ar(4s) + Ar$	$k_{(m^3/s)} = 5 \times 10^{-18}$	[35]
(R23) $Ar^+ + 2Ar \rightarrow Ar_2^+ + Ar$	$k_{(m^6/s)} = 2.5 \times 10^{-43}(T_g(K)/300)^{-3/2}$	[35]
(R24) $Ar_2^+ + Ar \rightarrow Ar^+ + 2Ar$	$k_{(m^3/s)} = \frac{6.06\times10^{-12}}{Tg(K)} \exp\left(-\frac{1.51\times10^4}{Tg(K)}\right)$	[27]
(R25) $Ar(4s) + 2Ar \rightarrow Ar_2^* + Ar$	$k_{(m^6/s)} = 3.3 \times 10^{-44}$	[30]
(R26) $Ar(4p) + 2Ar \rightarrow Ar_2^* + Ar$	$k_{(m^6/s)} = 3.3 \times 10^{-44}$	[35]
(R27) $Ar_2^* + Ar_2^* \rightarrow Ar_2^+ + 2Ar + e$	$k_{(m^3/s)} = 5 \times 10^{-16}(T_g(K)/300)^{1/2}$	[35]
(R28) $Ar_2^* + Ar(4s) \rightarrow Ar_2^+ + Ar + e$	$k_{(m^3/s)} = 6 \times 10^{-16}(T_g(K)/300)^{1/2}$	[35]
(R29) $Ar(4s) \rightarrow Ar + h\nu$	$\nu_{c(s^{-1})} = g_{eff}^a \times 3.145 \times 10^8$	[34]
(R30) $Ar(4p) \rightarrow Ar(4s) + h\nu$	$\nu_{c(s^{-1})} = 4.4 \times 10^7$	[34]
(R31) $Ar_2^* \rightarrow 2Ar + h\nu$	$\nu_{c(s^{-1})} = 6 \times 10^7$	[30]

[a] $g_{eff} = (1.15/\pi)\,(\lambda_{4s}/(6H))$, where $\lambda_{4s} = 105.7$ nm and H is a characteristic dimension of the reactor, i.e., taken as $H = 3$ mm in our case.

hand, considers the particle balance equations, the electron energy balance, the gas thermal balance and the Navier-Stokes equations for the gas flow description. In the following text we describe the equations used, as well as the boundary condition for every model. The axisymmetric model is of course defined in a cylindrical coordinate system and assumes zero azimuthal derivatives of all variables.

2.4.1. Particle balance equations The equations responsible for the plasma description (i.e. particle balance for electrons, the various ions and excited species, and electron energy balance) are the same in both models. We use the drift-diffusion approximation and we solve the well-known particle balance equation:

$$\frac{\partial n_s}{\partial t} + \nabla \cdot \boldsymbol{G}_s + (\boldsymbol{u}_g \cdot \nabla) n_s = S_c, \tag{1}$$

where n_s is the species density, $\boldsymbol{G}_s$ is the species flux, $\boldsymbol{u}_g$ is the gas velocity and S_c is the collision term representing the net number of particles produced or lost in the volume reactions included in tables 1 and 2. The index "s" represents all the species considered, except for the argon atoms, i.e. e, Ar^+, Ar_2^+, Ar (4s), Ar (4p), Ar_2^*. The argon gas atom density is considered to be constant.

The flux of the different species is expressed in the following way: the electron flux is

$$\boldsymbol{G}_e = -D_e \nabla (n_e) + \frac{q_e}{|q_e|} \mu_e n_e \boldsymbol{E}, \tag{2}$$

the ion flux is

$$\boldsymbol{G}_s = -D_s \nabla (n_s) + \frac{q_s}{|q_s|} \mu_s n_s \boldsymbol{E} \tag{3}$$

and for the neutral species ($\mathrm{Ar}\,(4\mathrm{s})$,$\mathrm{Ar}\,(4\mathrm{p})$ and Ar_2^*) the flux is only determined by diffusion: $\boldsymbol{G}_\mathrm{s} = -D_s\nabla\,(n_s)$. In the above expressions, D is the diffusion coefficient and, μ is the mobility of the corresponding species, $\boldsymbol{E}$ is the electric field vector and q_s is the charge of the given species type.

The transport coefficients used in the models are as follows: μ_e is derived from BOLSIG+ and the Ar^+ mobility is defined as in [36]:

$$\mu_{\mathrm{Ar}^+} = \frac{1.01\times10^5}{p_\mathrm{g}(\mathrm{Pa})}\frac{T_g(K)}{273.16}1.52\times10^{-4}\left(\mathrm{m}^2\mathrm{V}^{-1}s^{-1}\right), \tag{4}$$

where p_g is the gas pressure and T_g is the gas temperature. The latter expression is also used for the molecular ion mobility with a certain correction factor [36], i.e. $\mu_{\mathrm{Ar}_2^+} = 1.2\times\mu_{\mathrm{Ar}^+}$. The electron and ion diffusion coefficients are derived from their corresponding mobilities based on the Einstein relation. The $\mathrm{Ar}\,(4\mathrm{s})$ diffusion coefficient is defined according to [37] as

$$D_{\,\mathrm{Ar(4s)}} = (1/n_\mathrm{Ar})1.16\times10^{20}(T_{\,\mathrm{Ar(4s)}}(K)/300)^{1/2}\ \ (\mathrm{m}^2/\mathrm{s}), \tag{5}$$

and for the diffusion coefficients of $\mathrm{Ar}\,(4\mathrm{p})$ and Ar_2^*, due to the lack of literature data, we assume the same expression as for $\mathrm{Ar}\,(4\mathrm{s})$. This might look as a very rough approximation especially for Ar_2^*, but it does not affect significantly the final results because the diffusion terms in the balance equations for $\mathrm{Ar}\,(4\mathrm{p})$ and Ar_2^* remain negligible compared to the reaction terms. We also assume that the temperature of all heavy species is equal to the gas temperature (T_g).

2.4.2. Averaged electron energy balance The averaged electron energy is found by solving

$$\frac{\partial n_e\overline{\varepsilon}_e}{\partial t}+\nabla.\boldsymbol{G}_{\varepsilon,\mathrm{e}} + (\boldsymbol{u}_\mathrm{g}\cdot\nabla)n_e\overline{\varepsilon}_e = q_e\boldsymbol{E}.\boldsymbol{G}_\mathrm{e} + n_e\triangle\overline{\varepsilon}_e + Q_\mathrm{bg}, \tag{6}$$

where the electron energy flux is expressed as $\boldsymbol{G}_{\varepsilon,\mathrm{e}} = -D_{\varepsilon,e}\nabla\,(n_e\overline{\varepsilon}_e) - \mu_{\varepsilon,e}n_e\overline{\varepsilon}_e\boldsymbol{E}$. Here we use the following notations: $\overline{\varepsilon}_e$ is the electron averaged energy (averaged over the energy distribution function), $D_{\varepsilon,e}$ is the electron energy diffusion coefficient, $\mu_{\varepsilon,e}$ is the electron energy mobility and $\triangle\overline{\varepsilon}_e$ represents the averaged electron energy losses in the different collision events. $D_{\varepsilon,e}$ and $\mu_{\varepsilon,e}$ are derived from the electron mobility: $\mu_{\varepsilon,e} = (5/3)\mu_e$ and $D_{\varepsilon,e} = (2/3)\mu_{\varepsilon,e}\overline{\varepsilon}_e$. In order to make the numerical calculations more stable, we add a constant background power density Q_bg everywhere in the simulated domain (i.e. the plasma and the neutral gas). In this way, in the whole domain we artificially sustain a low density plasma ($n_\mathrm{e} < 1\times10^{16}\ \mathrm{m}^{-3}$) with a certain temperature derived self-consistently (around 1.8 eV in the bulk). This power density is low enough so that it does not affect the arc behaviour which is verified by several simulations with different background power Q_bg. The presence of background plasma allows us to significantly reduce the gradients in the variables between the arc and the background and thus to reduce the requirements to the discretization grid. The electron density due to this artificial heating is at least 4 orders of magnitude lower than the arc electron density.

2.4.3. Poisson equation The electric field in the discharge is calculated with the Poisson equation:

$$\triangle\Phi = -\rho_{\mathrm{q}}/\varepsilon_0, \tag{7}$$

where Φ is the electric potential, ρ_{q} is the charge density and ε_0 is the vacuum dielectric permittivity.

2.4.4. Gas flow equations For a proper description of the gliding arc we need to describe the gas flow which is responsible for the arc displacement. In the experiment considered here [20] the gas is supplied with a small nozzle positioned close to the shortest electrode distance position. With the 2D Cartesian model we are not able to describe accurately the gas flow from the nozzle. Therefore we solve here only a simplified version of the Navier-Stokes equations by adjusting the inlet boundary velocity in order to obtain a gas velocity similar to what is observed in the experiments. A rough estimation of the experimental gas velocity is obtained by examination of the arc displacement shown on successive high-speed photographs [20]. Note that this is, however, not a very accurate method since it is well possible that the arc does not have exactly the same velocity as the gas but slightly lower values [8,17]. Note that measurements in [17] show that the gas-to-arc velocity ratio is in the order of 1.2-1.3. The equations solved are the incompressible Navier-Stokes equations for a Newtonian fluid excluding the inertial term, i.e. in the regime of Stokes flow:

$$\rho_{\mathrm{g}}\frac{\partial \boldsymbol{u}_{\mathrm{g}}}{\partial t} = \nabla.(-p_{\mathrm{g}}\boldsymbol{I} + \mu_{\mathrm{g}}(\nabla\boldsymbol{u}_{\mathrm{g}} + (\nabla\boldsymbol{u}_{\mathrm{g}})^{\mathrm{T}})), \tag{8}$$

$$\rho_{\mathrm{g}}\nabla.\boldsymbol{u}_{\mathrm{g}} = 0, \tag{9}$$

where ρ_{g} is the gas density, p_{g} is the gas pressure, μ_{g} is the gas viscosity, $\boldsymbol{I}$ is the unit matrix and the superscript T stands for the tensor transpose operation. In the model, the Navier-Stokes equations are not solved together with the other equations, because this would yield excessive calculations times, but instead they are solved first separately and then the obtained velocity distribution is used as input data.

2.4.5. Gas thermal balance Gas heating is usually an important phenomenon in all arc discharges. Here we calculate the gas temperature by solving the gas thermal balance

$$\rho_{\mathrm{g}}C_p\frac{\partial T_{\mathrm{g}}}{\partial t} + \rho_{\mathrm{g}}C_p\boldsymbol{u}_{\mathrm{g}}.\nabla T_{\mathrm{g}} - \nabla.\left(k_{\mathrm{g}}\nabla T_{\mathrm{g}}\right) = Q_{\mathrm{g}}, \tag{10}$$

where C_p is the gas heat capacity of Ar, k_{g} is the Ar thermal conductivity and Q_{g} is a heat source, which in our case results from the plasma heating. This includes all the energy lost by the electrons in elastic and inelastic collisions, which is assumed to be finally transferred to the gas, as well as the energy transferred from the ions to the gas. The ions gain energy from the electric field. The total gas heat source is thus expressed as:

$$Q_{\mathrm{g}} = \frac{3m_e m_{Ar}}{\left(m_e + m_{Ar}\right)^2}n_e n_{Ar}k_1 e\left(T_e - T_{\mathrm{g}}\right) + \sum_i \triangle\varepsilon_i k_i n_e n_{i-t} + \boldsymbol{j}_{ion}\cdot\boldsymbol{E}, \tag{11}$$

where the first term represents the electron energy losses due to elastic collisions with rate coefficient k_1, the second term represents the sum of all electron energy losses due to inelastic collisions with energy loss $\triangle\varepsilon_i$, rate coefficient k_i and collision target density n_{i-t} for the i-th process, and the third term is the ion heating being the scalar product of the total ion current density $\boldsymbol{j}_{\rm ion}$ and the electric field $\boldsymbol{E}$. In the above expression the electron and gas temperatures are expressed in "eV". Here we neglect the energy loss due to radiation from excited atoms which is estimated to be relatively small (see also the comments in [25], page 277). The major term in equation (11) is usually the elastic energy transfer and only in the cathode layer the second and third terms in the right-hand side become considerable. The reason for the latter is the higher electron temperature in this region, enhancing the excitation processes, as well as the strong electric field which increases the ion velocity and the $(\boldsymbol{j}_{\rm ion}\cdot\boldsymbol{E})$ term.

2.4.6. Cathode thermal balance The cathode temperature is usually considered as a crucial parameter in arc discharges since it determines the thermionic emission from the cathode. The discharge considered here has a relatively low current and we could therefore expect only weak cathode heating. However the small area of the cathode spot could still lead to significant heating at the spot only. Therefore we examine the cathode heating by means of the heat balance equation:

$$\rho_c C_{p,c}\frac{\partial T_c}{\partial t} - \nabla.\left(k_c\nabla T_{\rm c}\right) = Q_c \tag{12}$$

where $\rho_{\rm c}$ is the mass density of the cathode material (2700 kg/m^3 for Al), $C_{\rm p,c}$ is the cathode heat capacity (900 J/(kg K) for Al), k_c is the cathode thermal conductivity (160 W/(m K) for Al), $T_{\rm c}$ is the cathode temperature in "K". The above coefficients are taken from material library integrated within the Comsol Multiphysics ® software. Q_c is the cathode heat source, due to resistive losses which are calculated from the current conservation equation:

$$\nabla\cdot\boldsymbol{J} = 0 \tag{13}$$

where $\boldsymbol{J} = (\sigma_{\rm c}+\varepsilon_r\varepsilon_0\frac{\partial}{\partial t})\boldsymbol{E}$ is the current density and $\sigma_c = \frac{\sigma_0}{1+0.0043(T_{\rm c}-293.15)}$ is the cathode conductivity with $\sigma_0 = 3.774\times10^7$ S/m for Al (taken from the material libray integrated within the Comsol Multiphysics ® package) and the cathode temperature $T_{\rm c}$ is taken in "K". The electric field is expressed as $\boldsymbol{E} = -\nabla\Phi_{\rm cons}$ where $\Phi_{\rm cons}$ is the potential distribution within the cathode. Hence, the cathode heat source is defined by Joule heating in the cathode: $Q_c = \boldsymbol{J}\cdot\boldsymbol{E}$.

In summary, the 2D axisymmetric model includes equations (1), (6),(7), (10), (12) and (13) while the 2D Cartesian model includes equations (1), (6)-(10).

2.5. Boundary conditions

Due to the relatively large number of equations, the number of boundary conditions (BC) is also large. They are summarized in tables 3 and 4, but some further explanation is given below.

The boundary condition for the electron balance equation (1) and the electron energy balance equation (6) at the cathode should include the electron emission processes in addition to the thermal flux. This yields the following BC for the normal electron flux at the cathode [38, 39]:

$$\boldsymbol{n} \cdot \boldsymbol{G}_{\mathrm{e}} = \frac{1}{2} \mathrm{v}_{\mathrm{e,th}} n_{\mathrm{e}} - \left[\sum_s \gamma_s \left(\boldsymbol{G}_s \cdot \boldsymbol{n} \right) + \boldsymbol{G}_{\mathrm{TF}} \cdot \boldsymbol{n} \right] \tag{14}$$

and for the normal electron energy flux [39]

$$\boldsymbol{n} \cdot \boldsymbol{G}_{\varepsilon,\mathrm{e}} = \frac{5}{6} \mathrm{v}_{\mathrm{e,th}} n_{\mathrm{e}} \overline{\varepsilon}_e - \left[\sum_s \gamma_s \varepsilon_{s,\mathrm{sec}} \left(\boldsymbol{G}_s \cdot \boldsymbol{n} \right) + \varepsilon_{\mathrm{TF}} \boldsymbol{G}_{\mathrm{TF}} \cdot \boldsymbol{n} \right] \tag{15}$$

In the above expressions $\mathrm{v}_{\mathrm{e,th}} = \sqrt{\frac{8 k_B T_e}{\pi m_e}}$ is the electron thermal velocity, γ_s is the secondary electron emission coefficient due to ion impact for the two types of ions (Ar^+ and Ar_2^+) having a normal flux $\boldsymbol{G}_s$ towards the cathode. Hence, the sum is taken over these two types of ions. k_{B} is the Boltzmann constant, m_e is the electron mass, $\varepsilon_{s,\mathrm{sec}}$ is the averaged energy of the secondary electrons and $\varepsilon_{\mathrm{TF}}$ is the averaged energy of the emitted electrons due to thermo-field emission. The value of γ_s is not known and it is very dependent on the cathode material and surface properties. In general, it could be calculated by fitting the model results to experimental results. In section 3.2 we will analyse its effect on the arc parameters and its value will be specified for every simulation. $\boldsymbol{G}_{\mathrm{TF}}$ is the electron flux due to thermo-field emission. It is known [40] that the combined effect of the thermal and field electron emissions (also denoted as thermo-field (TF) emission) is much stronger compared to the sum of both independent processes. Therefore, we use here the expression for the electron emission current density, which accounts for their combined effect [40]. It is also important to note that in the calculation of the field emission usually not the real normal electric field (E_n) is considered but an effective field which is calculated as $E_{n,eff} = \mathrm{FEF} * E_n$. The factor FEF is called "Field enhancement factor" and accounts for the effective enhancement of the field due to surface roughness and sharp protrusions [40]. Similarly to γ_s, this factor will be very dependent on a particular experiment and it may even change during the experiments because of surface modification as a results of the arc impact. Therefore in section 3.2 we will also examine the effect of FEF on the arc properties.

For the non-emitting walls (anode and $\mathrm{c_{up}}$) the BC includes only the thermal electron flux:

$$\boldsymbol{n} \cdot \boldsymbol{G}_{\mathrm{e,n}} = \frac{1}{2} \mathrm{v}_{\mathrm{e,th}} n_{\mathrm{e}} \tag{16}$$

The electron energy flux in this case is then:

$$\boldsymbol{n} \cdot \boldsymbol{G}_{\varepsilon,\mathrm{e}} = \frac{5}{6} \mathrm{v}_{\mathrm{e,th}} n_{\mathrm{e}} \overline{\varepsilon}_e. \tag{17}$$

The ion flux at the walls, for both the Ar^+ and Ar_2^+ ions, is found by accounting for their thermal velocity and their drift velocity due to the electric field:

$$\boldsymbol{n}\cdot\boldsymbol{G}_s = \frac{1}{4}\mathrm{v}_{s,\mathrm{th}}n_s + \max\left(\frac{q_s}{|q_s|}\mu_s n_s \boldsymbol{E}\cdot\boldsymbol{n}, 0\right) \tag{18}$$

where the function "max" returns the maximum of both arguments. In this case it sets the drift flux $\frac{q_s}{|q_s|}\mu_s n_s \boldsymbol{E}\cdot\boldsymbol{n}$ to 0 if it becomes negative, i.e. if the flux is directed towards the plasma domain. The neutral species, i.e. Ar(4s), Ar(4p) and Ar_2^*, are supposed to reach the wall due to thermal motion only and thus their BC on the wall is:

$$\boldsymbol{n}\cdot\boldsymbol{G}_s = \frac{1}{4}\mathrm{v}_{s,\mathrm{th}}n_s \tag{19}$$

where $s = \mathrm{Ar(4s)}, \mathrm{Ar(4p)}, \mathrm{Ar}_2^*$.

The cathode thermal balance considered in the axisymmetric model (non-gliding arc) requires also a boundary condition for the total heat flux at the cathode surface q_{cath}. We consider the following contributions:
1) Heat flux due to the ion kinetic energy mainly acquired in the cathode fall $\boldsymbol{q}_{\mathrm{i}} = \sum_s \boldsymbol{G}_{\mathrm{s}} 0.5 m_{\mathrm{s}} v_{\mathrm{s,n}}^2 + (3/2)k_{\mathrm{B}}T_{\mathrm{s}}$ where $s = \mathrm{Ar}^+, \mathrm{Ar}_2^+$, $v_{\mathrm{s,n}}$ is the normal ion velocity and m_{s} and T_{s} are their masses and temperatures.
2) Heat flux due to ion recombination on the walls. When an ion hits the wall it extracts an electron and recombines while releasing the rest of its internal energy (ionization energy 15.76 eV). The ion needs energy equal to the material work function ($W_{\mathrm{Al}} = 4.28$ eV) [41] in order to extract an electron from the cathode and we assume that the rest of the energy is deposited on the cathode. Thus we write $\boldsymbol{q}_{\mathrm{rec}} = e\sum_s \boldsymbol{G}_{\mathrm{s}}\left(U_s - W_{\mathrm{Al}}\right)$ where $U_s = 15.7$eV and 14.5eV for $s = \mathrm{Ar}^+, \mathrm{Ar}_2^+$ respectively. We should note that this expression is slightly overestimated since a small part of the energy could be carried away by the secondary electrons. Due to the small value of γ_s this effect is neglected.
3) Heat flux due to the electron flux. Despite the fact that the electrons are repelled by the cathode, some of them have enough energy to reach the cathode and contribute to the cathode heating $\boldsymbol{q}_{\mathrm{e}} = e\boldsymbol{G}_{\mathrm{e}}\left(\frac{5}{6}\overline{\varepsilon}_e + W_{\mathrm{Al}}\right)$.
4) Heat flux due to emission of electrons as a result of field emission. When electrons are extracted by the field emission, they heat or cool the cathode depending on the cathode temperature and electric field magnitude [40]. This is known as the Nottingham effect. To account for that effect we define an effective work function W_{eff} which is negative (cathode heating) or positive (cathode cooling) and it is again defined in [40]. The heat flux is thus written as $\boldsymbol{q}_{\mathrm{TF}} = -e\boldsymbol{G}_{\mathrm{TF}}W_{\mathrm{eff}}$.
5) Heat flux due to energy transfer from the hotter gas. The gas in front of the cathode spot is heated considerably due to electrons emitted by the cathode and accelerated by the cathode fall potential (in the order of 20 V). The conductive heat flux from the gas to the electrode surface is $\boldsymbol{q}_{\mathrm{g}} = -k_{\mathrm{g}}\nabla T_{\mathrm{g}}$.

Therefore, the total heat flux to the cathode is

$$\boldsymbol{n}\cdot\boldsymbol{q}_{\mathrm{cath}} = \boldsymbol{n}\cdot\left(\boldsymbol{q}_{\mathrm{i}} + \boldsymbol{q}_{\mathrm{rec}} + \boldsymbol{q}_{\mathrm{e}} + \boldsymbol{q}_{\mathrm{TF}} + \boldsymbol{q}_{\mathrm{g}}\right) \tag{20}$$

The current conservation equation (13) also requires the normal (perpendicular) current density at the cathode surface. It is expressed as the sum of the ion current plus the electron emission current due to TF emission and secondary electron emission, minus the electron flux towards the wall due to random motion, i.e.:

$$\boldsymbol{n}\cdot\boldsymbol{J} = |q_e|\boldsymbol{n}\cdot\left(\boldsymbol{G}_{\mathrm{Ar}^+} + \boldsymbol{G}_{\mathrm{Ar}_2^+} + \boldsymbol{G}_{\mathrm{TF}} + \gamma_s\left(\boldsymbol{G}_{\mathrm{Ar}^+} + \boldsymbol{G}_{\mathrm{Ar}_2^+}\right)\right) - |q_e|\frac{1}{2}\mathrm{v}_{e,\mathrm{th}} n_e \quad (21)$$

All these boundary conditions, as well as the other (more simple) boundary conditions, are summarised in tables 3 and 4.

Table 3. Boundary conditions used in the 2D Cartesian model, at the various boundaries (see figure 1); see text for the equation numbers. V_c is the cathode potential with respect to the grounded anode.

eq.	(1)	(1)	(1)	(6)	(7)	(8),(9)	(10)
variable	n_e	n_{Ar^+} $n_{\mathrm{Ar}_2^+}$	$n_{\mathrm{Ar(4s)}}$ $n_{\mathrm{Ar(4p)}}$ $n_{\mathrm{Ar}_2^+}$	$\overline{\varepsilon}_e$	Φ	$\boldsymbol{u}_\mathrm{g}$ p_g	T_g
$\mathrm{c}_{\mathrm{ins}}$	$\boldsymbol{n}\cdot\alpha = 0$; $\alpha = \boldsymbol{u}_\mathrm{g}$, $\boldsymbol{G}_\mathrm{s}$, $\boldsymbol{G}_{\varepsilon,\mathrm{e}}$, $\nabla\Phi$, ∇T_g						
c_c	(14)	(18)	(19)	(15)	$\Phi = V_\mathrm{c}$	$\boldsymbol{u}_\mathrm{g} = 0$	$T_\mathrm{g} = 293$ K
c_a	(16)	(18)	(19)	(17)	$\Phi = 0$	$\boldsymbol{u}_\mathrm{g} = 0$	$T_\mathrm{g} = 293$ K
$\mathrm{c}_{\mathrm{low}}$	$\boldsymbol{n}\cdot\alpha = 0$; $\alpha = \boldsymbol{G}_\mathrm{s}$, $\boldsymbol{G}_{\varepsilon,\mathrm{e}}$, $\nabla\Phi$					$\boldsymbol{n}\cdot\boldsymbol{u}_\mathrm{g} = 3$ m/s	$T_\mathrm{g} = 293$ K
c_{up}	(16)	$\boldsymbol{n}\cdot\nabla n_s = 0$		(17)	$\Phi = 0$	$p = 101$ kPa	$\boldsymbol{n}\cdot\nabla T_\mathrm{g} = 0$

Table 4. Boundary conditions used in the 2D axisymmetric model, at the various boundaries (see figure 1); see text for the equation numbers.

eq.	(1)	(1)	(1)	(6)	(7)	(10)	(12)	(13)
variable	n_e	n_{Ar^+} $n_{\mathrm{Ar}_2^+}$	$n_{\mathrm{Ar(4s)}}$ $n_{\mathrm{Ar(4p)}}$ $n_{\mathrm{Ar}_2^+}$	$\overline{\varepsilon}_e$	Φ	T_g	T_c	Φ_{cons}
$\mathrm{a}_{\mathrm{p,ins}}$	$\boldsymbol{n}\cdot\alpha = 0$; $\alpha = \boldsymbol{u}_\mathrm{g}$, $\boldsymbol{G}_\mathrm{s}$, $\boldsymbol{G}_{\varepsilon,\mathrm{e}}$, $\nabla\Phi$, ∇T_g							
$\mathrm{a}_{\mathrm{c,ins}}$ $\mathrm{a}_{\mathrm{c,out}}$							$T_\mathrm{c} =$ 293 K	$\Phi_{\mathrm{cons}} =$ 0
a_c	(14)	(18)	(19)	(15)	$\Phi = V_c$	$T_\mathrm{g} = T_\mathrm{c}$	(20)	(21)
a_a	(16)	(18)	(19)	(17)	$\Phi = 0$	$T_\mathrm{g} = 293$ K		
$\mathrm{a}_{\mathrm{axis}}$	$\boldsymbol{n}\cdot\nabla\alpha = 0$; $\alpha = n_\mathrm{s}$, $n_\mathrm{e}\overline{\varepsilon}_e$, Φ, T_g, T_c, Φ_{cons}							

Finally, we need to specify certain conditions for the external circuit and the power supply. There must be an element in the circuit which limits the current through the arc. In the experiment under consideration, the power supply is a high voltage neon light transformer which has considerable inductance thus playing the role of ballast inductance. Due to the lack of data about the exact transformer parameters (mutual

inductance, primary and secondary coils, etc.) we simplify the circuit by assuming that the current is limited by a simple resistor R_{b}. The voltage source is constant in the case of the axisymmetric model ($V_{\mathrm{source}} = 3500\ V$) and it has a sinus shape for the Cartesian model $V_{\mathrm{source}} = 3500 \sin(2\pi 50t + 0.25)\ V$. The cathode voltage V_{c} is calculated from the Ohm's law based on the value of the total arc current at the cathode. Note that the voltage drop (and thus the resistance) of the cathode layer is self-consistently calculated within the model by the Poisson equation. This avoids the need of analytical layer representations but of course it comes with an increased computational cost. The 2D cartesian model can consider a complete period of the power supply voltage or even several cycles. However in the simulation results presented in this work we will consider only one half cycle of the voltage source, i.e. a DC mode of operation. There are two reasons for that: (1) The geometry is symmetrical. (2) The obtained results show that there is no interaction between consecutive arcs created during the different voltage polarities or even within the same polarity (half period). For the considered experiment the latter becomes possible only for high gas flow (i.e. 10 slm) [20] when the arc extinguishes because it becomes too long for a time less than half of the voltage period (10 ms) and the voltage is still enough to ignite a new arc [20, 21]. In the AC regime the consecutive arcs will not differ from each other because the electrodes are identical and thus the voltage polarity will only change the current direction but not the arc parameters. The above approach is based on the observations of the experimental arc motion [20,21]. We should note, however, that in the AC regime it might be possible that if an arc is ignited close to the moment of polarity reversal, the arc will be extinguished when the voltage drops. Thus there will be a decaying residual low density plasma moving downstream with the gas. If the channel is conductive enough, the subsequent breakdown (due to reverse polarity voltage increase) can take place within this channel instead of at the position of the shortest electrode distance. This situation is not yet considered in our model.

3. Results and discussions

In this section, we present several results addressing different aspects of the discharge operation and demonstrating the advantages and limitations of the applied modelling approach.

3.1. Electrode heating - cold or hot cathode arc (2D axisymmetric model)

The electrode heating is analysed in order to determine the regime of discharge operation with respect to the cathode electron emission, i.e. to determine whether the cathode heats up or stays cold. Furthermore, when the cathode stays cold, this is important information for the development of the 3D model, as it will help to reduce the computational cost of the gliding arc model by excluding the electrode thermal balance equation. Electrode heating is certainly important in high current arcs mainly due

to the thermal electron emission considered as a primary mechanism for the discharge sustainment. On the other hand, low current arcs, like the one considered here, probably will not be able to heat the whole electrode, but still the electrode temperature could locally be relatively high at the cathode spot due to its very small size and high current density. Indeed, arcs with relatively cold cathodes generally form cathode spots in order to provide higher electric fields in the cathode layer for efficient field electron emission or/and higher surface temperature locally at the spot [12] due to the exponential increase of the electron emission with increasing electric field and temperature. A quantitative analysis is thus necessary, and for that purpose we use the axisymmetric model (i.e. non-gliding arc) which includes a detailed description of the heat fluxes towards the cathode and the Joule heating. Here we assume that if a non-gliding (stationary) arc does not heat the electrode, a gliding arc having the same total current would certainly not be able, since the latter moves along the electrode and the heat is better redistributed, i.e. the electrode should even be colder.

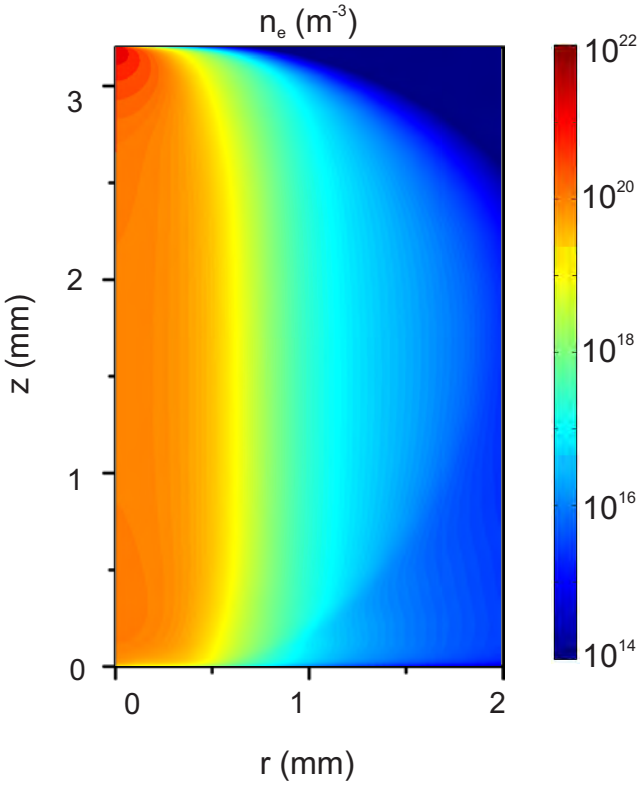

Figure 2. Electron density distribution, calculated with the axisymmetric model for the following parameters: $I_{\mathrm{ga}} = 31$ mA, FEF $= 100$, $\gamma_s = 0.01$, $R_{\mathrm{b}} = 110$ kΩ, $t = 1$ ms. The anode is found at $z = 0$, whereas the cathode is positioned at $z = 3.2$ mm.

Figure 2 shows the calculated electron density distribution for the parameters mentioned in the figure caption. The ballast resistor $R_{\mathrm{b}} = 110$ kΩ is chosen so that it provides a total arc current $I_{\mathrm{ga}} = 31$ mA, which is similar to the typical experimental value [20]. At the cathode ($z = 3.2$ mm) the arc forms a small cathode spot, giving rise to a maximum in the electron density at the symmetry axis (see figure 2). The

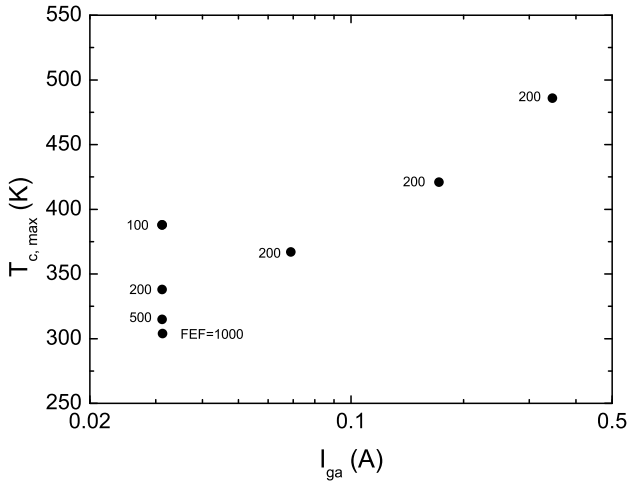

Figure 3. Maximum cathode temperature as a function of total arc current $I_{\rm ga}$. The assumed FEF values are denoted on the figure near every point. The other parameters are $\gamma_s = 0.01$, $t = 1$ ms.

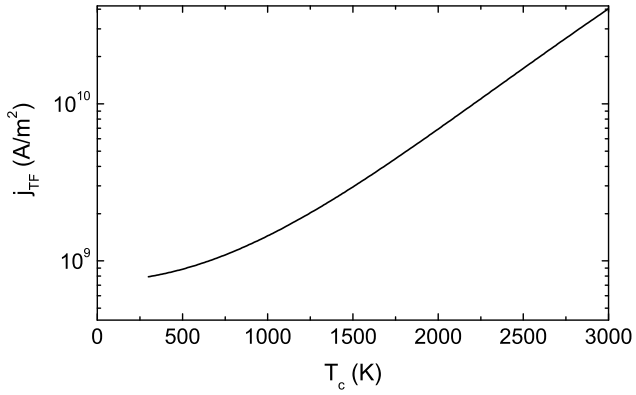

Figure 4. Thermo-field electron current density as a function of cathode temperature for a fixed electric field of 4×10^7 V/m, FEF = 100, $\gamma_s = 0.01$ and $W_{\rm Al} = 4.28$ eV.

peak cathode temperature calculated at this position, $T_{\rm c,max}$, is plotted for different arc current values in figure 3. Near every point on the figure we also denote the assumed FEF value. The arc current is varied by varying the ballast resistance $R_{\rm b}$. For the lowest current, several results are depicted, corresponding to different FEF values. As we will see in the next subsection, lower FEF values result in smaller cathode spots and thus higher current densities, and this will give rise to more intensive heating and thus higher local temperatures at the cathode spot.

As a whole, the cathode temperature remains relatively low (below 600 K) even for arc currents being 10 times higher than the typical experimental values. The temperature is considerably lower than the typical values for high current arcs with hot cathode (above 1500 K [12]). As mentioned above, this is important information for the development of the 3D model, as it means that we can exclude the electrode thermal balance equation in the 3D model, which will reduce the computational cost.

In order to quantify the influence of the obtained maximum cathode temperature ($T_{\mathrm{c,max}}$) on the electron emission, we evaluate the electron emission current density ($q_{\mathrm{e}}G_{TF}$) as a function of T_{c} for a fixed electric field; see figure 4. The electric field value is taken from the model results at the cathode on the discharge axis (i.e. peak value) and it is 4×10^7 V/m for the case of $I_{\mathrm{ga}} = 31$ mA, FEF = 100, $\gamma_s = 0.01$. The thermo-field electron emission current density shows a weak dependence on the cathode temperature at low T_{c} values and starts rising faster above 1500 K. As our calculated cathode temperature is well below 1500 K, we may conclude that the thermo-field emission can be considered for constant cathode temperature (i.e. cold cathode operation) for the discharge conditions under study. Of course, as in every model, the above treatment has certain limitations. In our opinion the primary limitation is the lack of any information in the model about the electrode surface roughness and the existence of small protrusions. As we already mentioned, they could lead to a higher electric field and thus higher current densities. Moreover, such structures will have a different thermal balance compared to the above treatment (assuming a flat surface) due to the smaller contact surface with the electrode body, leading to reduced thermal conduction. These factors could result in higher local temperatures. However, we cannot really account here for such effects because the surface properties could even be modified from the discharge itself as a result of sputtering.

3.2. Influence of the field enhancement factor (FEF) and the secondary electron emission coefficient (γ_s) (2D axisymmetric model)

In the description of the boundary conditions for the electron emitting cathode we noted that there are two unknown external parameters that need to be specified in the model, i.e., FEF and γ_s. Both of them are very dependent on the particular surface and operating conditions. The best solution will be to adjust the γ_s and FEF coefficients until the model results fit to the experimental current and voltage values. However, fitting over two parameters can result in multiple solutions. Therefore, instead of fitting, we limit here our treatment to the demonstration of their effect for a steady non-gliding arc, i.e. we use again the axisymmetric model.

Figure 5 shows the dependence of the obtained discharge power and the cathode spot diameter on the chosen FEF, for a fixed $\gamma_s = 0.01$ and arc current of $I_{\mathrm{ga}} = 31$ mA. Lower FEF values mean that the real electric field at the cathode needs to be higher in order to supply the same current. This is well seen from the potential profile along the arc axis (figure 6) which shows a large voltage drop and gradient near the cathode for low FEF values (100 in this case). The higher voltage drop results in a higher arc voltage and thus in a slightly higher total discharge power at low FEF, as can indeed be deduced from figure 5. Physically, the increased electric field is achieved by shrinking the cathode spot to a diameter as small as 6 μm for FEF = 100 (see figure 5), and the maximum current density becomes then around 10^9 A/m^2. The cathode spot diameter d_{spot} is defined as $d_{\mathrm{spot}} = 2I_{\mathrm{ga}}/\left(\pi \max(\boldsymbol{n} \cdot \boldsymbol{J})\right)$ where $(\boldsymbol{n} \cdot \boldsymbol{J})$ is the current density normal

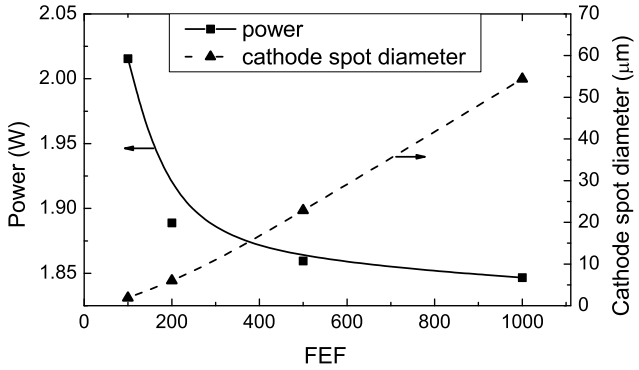

Figure 5. Discharge power and cathode spot diameter, calculated for different values of FEF. $I_{\rm ga} = 31$ mA, $\gamma_s = 0.01$, $R_{\rm b} = 110$ kΩ, $t = 1$ ms. The lines are spline fit.

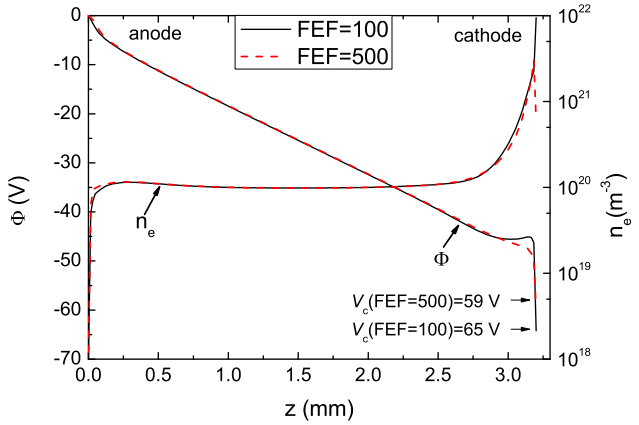

Figure 6. Electron density and potential variation between anode and cathode, along the symmetry axis, for two values of FEF. $I_{\rm ga} = 31$ mA, $\gamma_s = 0.01$, $R_{\rm b} = 110$ kΩ, $t = 1$ ms

to the cathode. Note that the cathode spot diameter varies more or less linearly with the assumed FEF values. At low FEF values the power increases almost exponentially and the cathode spot becomes so small that it is in the order or even smaller than the cathode fall thickness (i.e. $d_{\rm spot} \simeq 6\ \mu m$ and cathode fall thickness $15 - 20\ \mu m$ at FEF=100; see figure 5). For FEF values below 100 the simulation becomes unstable and the discharge tends to transform into a glow discharge. Low FEF values correspond to a glow discharge regime, where the electron emission is provided mainly by secondary electron emission due to ion bombardment. Our model is capable of reproducing a glow discharge, but we have not focussed on this regime because the images of the considered experiments [20,21] clearly show that the discharge is in the arc regime (there is no wide cathode spot). It was also stated in literature [4] that if no special treatment is applied to the cathode for reduction of the FEF coefficient, the transition to an arc discharge appears at relatively low current values (below 30 mA) in argon [4]. The values of the FEF coefficient (higher than 100) considered here are indeed typical for electrodes without special treatment [42]. Note that if a different gas would be used, the discharge

could be in a glow mode even for currents in the order of 100 mA [6, 7].

Figure 6 yields also another important result. Despite the sensitivity of the cathode fall and cathode spot on the FEF values, the remaining part of the arc is practically not affected, as can be observed from both the potential profile and the electron density in figure 6. Indeed, the current value is what determines the plasma properties of the arc body and anode region, while the FEF value affects the cathode fall which adapts in order to supply the current fixed by the external circuit. This result is also very important, as it gives an option for the reduction of the computation cost of the gliding arc discharge modelling in 3D. Using larger FEF values leads to larger cathode spots, and hence lower electric fields, and thus lower requirements for the mesh resolution in the cathode region, while the remaining part of the arc is not affected. The "price" will be that the discharge power/voltage for the same current will be probably underestimated.

The strong dependence of the cathode spot diameter on the FEF values indicates that the secondary electron emission coefficient (γ_s) has a small contribution to the electron emission. This is confirmed by the analysis of the model results with different values of γ_s for the smallest attainable FEF of 100 (note that for higher values of FEF the effect of secondary electron emission is even smaller). The contribution of the secondary electron emission remains negligible even for γ_s values up to 0.3. The latter value is already much too high for most of the cathode materials and thus we can completely ignore the effect of secondary electron emission. Hence the above analysis shows that the dominant mechanism of cathode electron emission in our case is the field emission. The real value of the FEF coefficient is very dependent on the experimental conditions and it should be adjusted within the model in order to obtain the experimental values of the arc voltage and current.

3.3. Gliding Arc - arc roots displacement (2D Cartesian model)

One of the most distinct features of gliding arc discharges is their ability to glide along the electrodes. The gliding mechanism, however, is still not well understood. Based on the results from our axisymmetric model (figure 2) and experimental observations in the literature, we know that the contact points of the arc with the cathode and the anode (i.e. the so-called arc roots) have rather different properties. At the anode, the arc has a relatively wide diffusive contact area while at the cathode a tiny spot is formed. Fast imaging of the discharge [20] shows that at least in the initial stage of the arc travel along the electrodes, the arc roots follow the displacement of the arc body (as a result of the gas flow drag). However, if we expect that the arc moves due to the gas flow only, we should observe a much slower velocity of the arc roots compared to the arc body, since the gas velocity has a maximum value at the discharge axis and gradually decreases to zero at the electrode surface. Apparently this is not the case and therefore it is clear that another mechanism contributes to the arc roots displacement.

In several experimental studies, rather different types of arc roots gliding are reported for the cathode and anode. It is shown in [20, 43–45] that the arc is rather

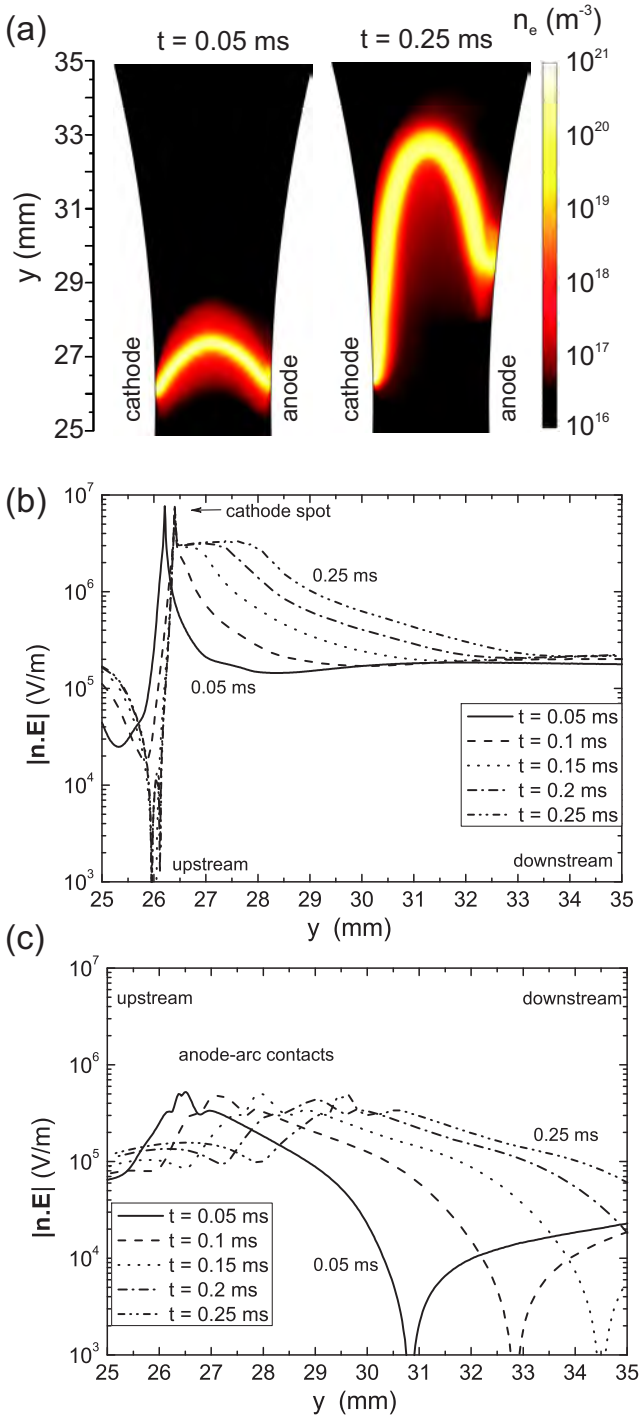

Figure 7. (a) Electron density in the arc for two different moments, i.e. $t = 0.05$ ms and $t = 0.25$ ms. Magnitude of the normal electric field in front of the cathode (b) and anode (c). Conditions: FEF = 400, $\gamma_s = 0.02$, arc current 30.2 A/m, source voltage $V_{\text{source}} = 3500 \sin(2\pi 50t + 0.25)$ V, $R_{\text{b}} = 30$ Ω/m.

smoothly gliding at the anode, while the cathode spot is jumping from one point to another. In our simulations with the 2D Cartesian model we observe a similar behaviour. Figure 7(a) shows the arc evolution in time from 0.05 ms to 0.25 ms, for simulation

parameters providing an electron density in the arc close to the values obtained from the axisymmetric model, calculated with the experimental current value. The FEF parameter is chosen relatively large in order to increase the cathode spot size and facilitate the calculations. γ_s is given a typical value of 0.02, although secondary electron emission does not play any role. We observe a slow or immobile cathode spot (at the left) and a smoothly gliding anode arc root (at the right).

To easily analyse this behaviour, we also plot the electric field magnitude at the cathode and anode surfaces (figure 7(b) and (c), respectively). Note that the electric field values outside the contact zones are not reliable, as they are the result of the artificially sustained low density plasma in the whole domain, which does not exist in reality. For example, the electric field above the anode root becomes negative due to the formation of a positive plasma potential in the expansion zone above the electrodes. Hence, we should only focus at the electric field values near the contact zones.

The electric field variation in front of the cathode (figure (7(b)) clearly shows the formation of a cathode spot, characterized by a sharp peak of the electric field. The cathode spot is weakly affected by the arc displacement. To understand why, we need to remind that the strong electric field at the cathode spot is formed in the cathode fall, which has a thickness in the order of 20-50 μm for this simulation. The gas velocity in this zone remains about 10 times lower compared to the discharge centre (2-3 m/s vs. 32 m/s maximum velocity). As a result, the drag of the cathode layer (and spot) by the gas flow will be very small. In this particular simulation, the cathode spot moves around 200 μm for 0.05 ms, and then it stops (see figure 7(b)). It seems that the spot is very sensitive to the "surface imperfections", in our case related to the mesh inhomogeneity. In the model the cathode surface is smooth, but the discretization mesh has small variations from the desired size (2 μm). The spot stops at a point where the mesh is slightly finer, which allows numerically a higher electric field to be established in the solution. Due to the highly non-linear TF electron emission, this point seems to be more advantageous than the next cells of the mesh, providing a lower electric field and thus lower current density. We suspect that a real cathode spot will have a similar behaviour and it will attach to surface protrusions, providing a higher local electric field. Using even a finer mesh in the model at the cathode surface probably will allow a smooth self-consistent cathode spot motion. However, this will require significant computational resources and it is not justified, taking into account that it is not very realistic, as shown by experimental observations [20, 43–45].

Furthermore, we can deduce from figure 7 (b), that with the arc prolongation downstream, the electric field at the cathode above the cathode spot (i.e., in the direction of the gas flow) is rising. If that field becomes strong enough, a new breakdown can occur at that position and the old part of the arc will vanish, due to the shorter arc length provided by the new cathode spot. In the present simulation this field value is not strong enough to cause a new breakdown due to the very non-linear dependence of the field emission on the electric field. However, in real experiments the arc shape is not so smooth and the surface is not perfectly flat as in our simulation. If there are

surface protrusions (causing a local increase of the field) or if the arc has an irregular shape leading to a shorter distance between the arc and the cathode (as shown in [43], figure 9), a breakdown can occur at that point and a new cathode spot can be formed. This process would represent a "jump" of the cathode spot. Note that this behaviour will be mimicked in section 3.4 below.

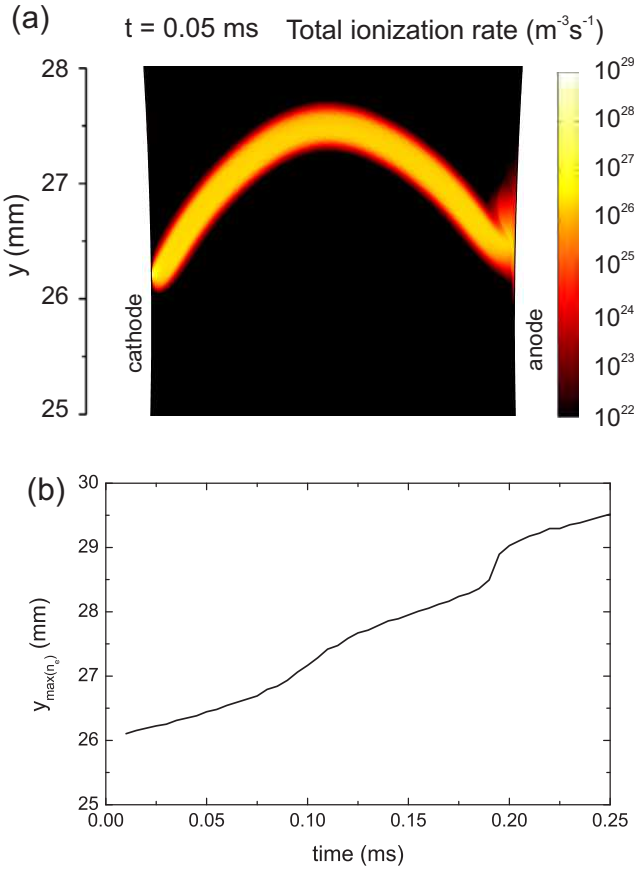

Figure 8. Total ionization rate (sum over all ionization processes), showing the increased ionization in the downstream zone above the arc-anode contact point (a), and "y" position of the electron density maximum at the anode as a function of time (b). The simulation conditions are the same as in figure 7.

The anode-arc connection has a rather different behaviour (figure 7 (a)). The current channel and the electric field have also a well pronounced maximum at the anode (figure 7 (c)) but the size of the contact zone is much larger – around 1 mm (defined in the same way as for the cathode spot size; cf. section 3.2 above). Moreover, the electric field is more than an order of magnitude lower compared to the value at the cathode spot. When the angle between the arc and the anode becomes less than 90 degrees (i.e. when the arc is bended due to gas drag), the electric field at the anode above the anode-arc contact is becoming higher (figure 7 (c)), and the smaller the angle, the higher is the electric field. As a result, the electrons start to ionize more and more in the downstream zone above the contact point, as is illustrated in figure 8(a), and effectively they extend the current channel downstream. The newly created conducting

area provides a shorter path for the electrons to the anode and thus the current channel moves gradually downstream, as is illustrated by the moving "y-position of maximum electron density" as a function of time in figure 8 (b). In this way, the anode root displacement is not directly related to the gas flow velocity, but it is rather a result of the arc bending, caused by the gas flow. The variation of the displacement speed of the anode-arc contact point, which can be observed in figure 8 (b) at approximately 0.19 ms, is not an abrupt jump but it is a consequence of the variation of the anode spot size. For some reason the contact zone becomes larger around 0.19 ms and then shrinks again. When the contact zone is larger, the maximum of the electron density is not well-pronounced which results in a variation of the calculated displacement velocity.

The big difference in the behaviour of the cathode and anode spots is due to the size of the contact zone and due to the current dependence on the electric field. Indeed, at the anode the current is a result of an electron drift being linear with respect to the electric field while at the cathode it is determined by the field emission which is highly non-linear with respect to the electric field.

The above behaviour should be mainly valid for low current gliding arc discharges in arc mode (i.e., current up to several hundred of milliamperes). In higher current arcs it is often found that the cathode spot is quasi-randomly moving all the time due to heating and melting of the cathode and due to micro-explosions within the spot [12]. Hence, in high current GADs, such processes may occur and thus the mechanisms of cathode spot displacement could be different from what is presented here. In this case, it could be determined not by the breakdown between the arc and the electrode (as considered here) but by a quasirandom motion of the spot, being quasi and not fully random due to gas flow and the arc bending.

3.4. Gliding Arc - general behaviour (2D Cartesian model)

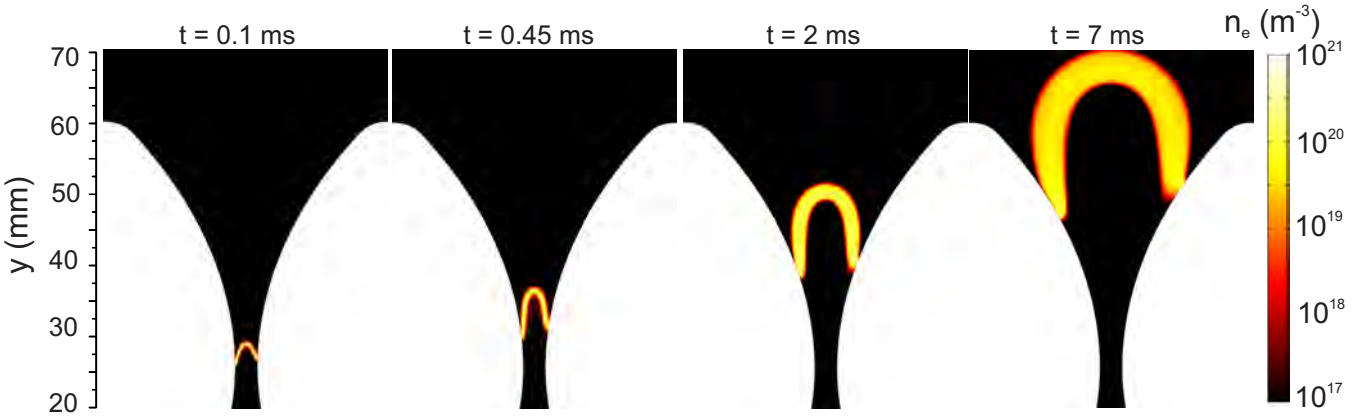

Figure 9. Electron density at different moments of the arc evolution, representing a complete cycle of a single arc gliding. Conditions: FEF = 400, $\gamma_s = 0.02$, arc current 30.2 A/m, source voltage $V_{\text{source}} = 3500 \sin(2\pi 50t + 0.25)$ V, $R_{\text{b}} = 30$ Ω/m

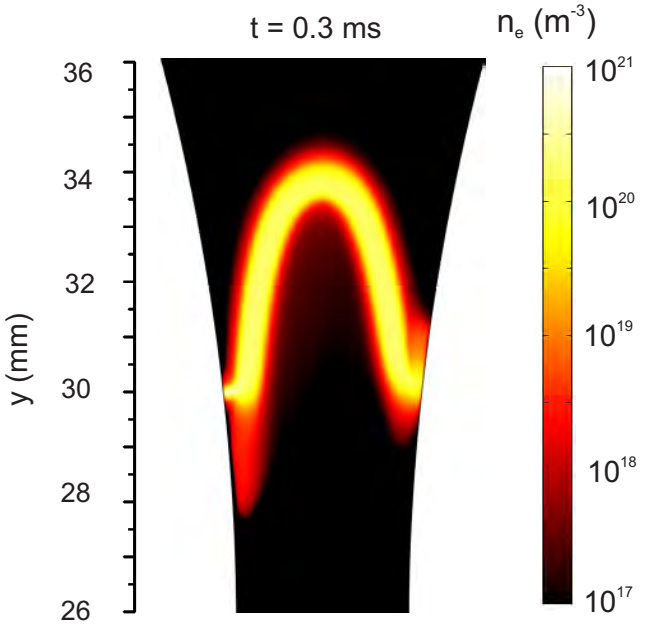

Figure 10. Electron density at 0.3 ms during the cathode spot displacement (jump). A new spot is initiated and the old one diminishes since the new spot provides a shorter arc length. The conditions are the same as in figure 9.

Keeping in mind the above described behaviour of the cathode spot in our simulations, it is clear that in order to simulate the arc gliding we need to enforce it somehow to move and follow the arc body. The approach chosen here is based on a controllable displacement of the cathode spot following the anode contact point. This is done by defining the FEF coefficient to take a non-zero value only in a limited region several times larger than the cathode spot, i.e. the breakdown is possible only within this region. In practice we apply the following algorithm. Initially (at time $t < 1$ μs) we create a small (1-2 mm) plasma channel at the shortest electrode gap (position $y = 26$ mm in our case) by applying a certain power density profile and we set the FEF value to be non-zero at the same position. Subsequently we apply the external voltage, the gas in the discharge gap breaks down and the initial arc is established. Due to the drag by the gas flow, the arc is bended downstream and the anode arc root moves upwards, as explained in section 3.3 above. When the anode arc root moves a few millimetres (2-3 mm), we set a second non-zero FEF value at a point downstream, corresponding to the position of the anode arc root, where another cathode spot will be initiated. To facilitate the breakdown, we set this FEF to a very high value (5000) for a short time, so that the electric field at this position is sufficient to cause the breakdown. When the new spot is formed, the old one vanishes and the arc is moving forward. The procedure is repeated (typically 7-10 times) during the arc gliding downstream until it vanishes due to the very long arc length or the drop of the external voltage. In this procedure the cathode spot follows the anode arc root, which is calculated self-consistently. Figure 9 shows the modelling results for the time evolution of a gliding arc

discharge performed with the above procedure, while figure 10 gives a zoom over the cathode spot displacement at $t = 0.3$ ms.

Numerically, the whole simulation is divided into several subperiods corresponding to every cathode spot jump and having a different mesh. Every mesh is highly inhomogeneous with element sizes of 5 μm at the two spots (old and new) and around 80 μm in the area where the arc body passes. The meshing is done manually. Comsol Multiphysics has an adaptive mesh refinement but we were not able to obtain satisfactory results using that option.

It is also possible to simulate the cathode spot gliding in a smooth and controllable way. If we define again the FEF factor in a limited region slightly larger than the cathode spot, we can move the FEF profile smoothly downstream and the cathode spot will be forced to follow this. As we already mentioned, the experimental observations do not support such behaviour [20, 43–45] and moreover, this approach seems to be numerically more difficult. Indeed the mesh should be very fine along the whole path of the spot and the time step becomes limited to small values. Therefore, our numerical experiments show a considerably longer computation time compared to the procedure with jumping spot.

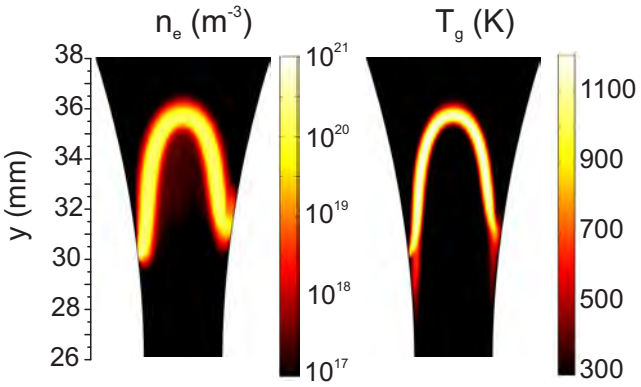

Figure 11. Electron density n_e and gas temperature T_g at $t = 0.4$ ms. The conditions are the same as in figure 9.

Another interesting result follows from the mechanisms of the arc roots displacement. As mentioned in the previous subsection, the arc near the electrodes is moving considerably faster than the background gas in this region. As a result it leaves behind a trace of hot gas near the electrodes. This effect is demonstrated in figure 11, showing the gas temperature distribution and the electron density (representing the arc) at the same time. In the case of a highly turbulent gas flow, the above effect probably will be reduced, especially near the anode, since the turbulent gas flow leads to higher velocity gradients near the wall.

With respect to the arc body velocity, several experimental studies have shown that it could be slightly lower than the gas velocity [8, 17]. The difference is usually 1.1-1.3 times and is very dependent on the gas velocity value, the applied power and even the arc length [8, 17]. Usually the difference is higher for higher gas flow velocities and it

decreases with the increase of the arc length. While not perfectly clear, the reason for the arc body lag is related to the instabilities of the arc and secondary breakdowns causing arc length reduction [46]. It has been shown in several experiments [8, 17, 20, 21] that the arc voltage exhibits sharp drops during its movement downstream. Fast imaging of the discharge reveals that in many cases the discharge is unstable and it has a rather irregular shape. The voltage fluctuations were ascribed to so-called back-breakdown phenomena [46] which is the fast shortening of the arc as a result of breakdown between different parts of the arc (i.e., not between the electrodes). If we look again at figure 7 (a), we can see that below the top of the arc, there is a zone with density in the order of 10^{18} m^{-3} and higher. If the arc continues to elongate, the voltage will also increase and the density in this region might be sufficient for a breakdown, reducing the arc length. These shortcuts effectively appear as a lag of the arc velocity compared to the gas flow and could be an efficient mechanism for gas cooling since in this way the heat is spread over a larger domain and not only within the arc channel.

This effect is not taken into account in the results presented above. Since it is mostly stochastic by nature and it is not well defined, we are not able to describe it directly in our model. Instead we take an indirect and rather rough approach by defining a coefficient equal to the ratio of the arc and the gas velocity ($\alpha_{\mathrm{lag}} = \boldsymbol{u}_{\mathrm{arc}}/\boldsymbol{u}_{\mathrm{g}}$) and we use it to multiply the convection velocity in the particle balance and electron energy balance equations, i.e. instead of $\boldsymbol{u}_{\mathrm{g}}$ in equations (1) and (6) we use $\alpha_{\mathrm{lag}}\boldsymbol{u}_{\mathrm{g}}$. Taking $\alpha_{\mathrm{lag}} = 0.75$ and running again the model used for figures 9 and 11, we find that the plasma parameters (n_{e} and T_{e}) and the gas temperature are hardly changed. Quantitatively the influence of the arc lag will be studied in detail in our future 3D calculations.

4. Conclusions

In this work we report on modelling of a gliding arc discharge in argon. Even with certain approximations, the self-consistent description of the discharge requires coupling of a large number of equations, accounting for plasma formation, gas and cathode heating, gas flow, and electron emission processes. The complexity of the model and the necessary computer time for full 3D calculations (i.e., more than a month for a single run) provoked us to evaluate certain aspects of the discharge operation with 2D models. These 2D models are found to be very useful and capable of giving a lot of information on the discharge behaviour, which otherwise would take a long time to gather. We developed two different types of 2D models – an axisymmetric and a Cartesian model.

Based on the axisymmetric model we have studied the cathode heating and the influence of the surface properties on the arc behaviour. For the considered low current arc in argon, the cathode remains cold (below 500 K) even when very tiny cathode spots are established and thus the field emission is the main electron emission mechanism. The analysis of the effect of the cathode properties on the model results shows that the unknown FEF factor may have a considerable impact on the obtained overall discharge

power and on the arc cathode fall. Lower FEF values result in very tiny cathode spots (several micrometers in diameter) and to large voltage drops within the cathode fall. The remaining part ot the arc, however, is practically not influenced. The real value of FEF for a particular experiment is usually unknown and when modelling such a discharge the value could be adjusted until acceptable conformity with the experiment is obtained.

Using the 2D Cartesian model we have studied qualitatively the arc drag by the gas and the arc gliding along the electrodes. As shown in several experiments with low current gliding arc discharges, the arc-cathode and arc-anode contact points have rather different behaviour. At the anode there is a wide contact zone and its displacement downstream is governed by the arc bending and the induced asymmetry in the electric field near the surface. At the cathode, the cathode fall determining the electron emission is very compact and in practice it is only affected by the gas flow there. The gas velocity near the surface is very small which leads to a very slow displacement of the cathode spot. Moreover, as a result of highly non-linear TF electron emission, in real devices the cathode spot will tend to attach to surface protrusions producing zones with increased electric field. In order to follow the arc body, the cathode spot "moves" by the establishment of new spots downstream (new breakdowns) which resembles jumping along the cathode surface. To model this behaviour we enforce the cathode spot to follow the arc-anode contact by controlling the spot position and reignition. The latter is done by setting a certain time and spatial shape of the FEF factor. The algorithm is demonstrated in the simulation of a complete arc cycle – from initial ignition to decay. The model shows that there is no interaction between the successive gliding arcs. With respect to gas treatment application of GADs, this would mean that a certain amount of gas remains untreated, even taking into account the differences in the gas and arc velocities. This will be investigated in our future work.

In this work we have not included a detailed comparison with experimental data since the models presented here cannot yet quantitatively treat the real gliding arc discharge. We can expect a quantitative match with the experiment only for results based on a full 3D model. However, we have tried to compare the results with experimental data from emission spectroscopy [20], providing values for the electron density and the gas (rotational) temperature at the discharge axis. The comparison of the absolute values of the above parameters obtained by the axisymmetric model (figure 2) with the experimental ones - shows that the electron density obtained in the model is more than one order of magnitude lower and the gas temperature (not shown in the manuscript) is almost twice as high (around 1000 K). This is expected since the axisymmetric model lacks a gas flow and we could expect that the arc extension and the gas flow (which is close to turbulent) will enhance the gas cooling processes (i.e. the gas temperature will be lower). Probably this will lead to a stronger contraction of the plasma column and eventually to higher density values. This shows indeed that the present 2D model is not yet quantitatively correct. However, we were able to qualitatively reproduce the arc gliding process shown in [20]. Therefore, we may

conclude that our model already gives a good qualitative insight in the underlying processes, and we hope to capture the gas flow effects in the 3D model that is under development.

Finally we would like to note that using a different gas for the same current range may produce not only quantitatively but also qualitatively different results. As it is shown in [4, 5], depending on the gas and the current value, the discharge might be in a glow or arc discharge mode. The glow discharge has a rather different structure and the gliding mechanism will be different.

5. Acknowledgements

This work is financially supported by the Methusalem financing. The work was carried out in part using the Turing HPC infrastructure of the CalcUA core facility of the Universiteit Antwerpen, a division of the Flemish Supercomputer Center VSC, funded by the Hercules Foundation, the Flemish Government (department EWI) and the Universiteit Antwerpen. Finally, the authors would like to thank X. Tu and J. C. Whitehead for the valuable discussions and for providing insight in the experiments.

References

[1] Fridman A 2008, *Plasma Chemistry* (Cambridge: Cambridge University Press)
[2] Chernichowski A 1994 Gliding Arc. Applications to engineering and environment control *Pure and Appl. Chem.* **6** 1301-1310
[3] Sprott J 2006 *Physics Demonstrations: A Sourcebook for Teachers of Physics* (University of Wisconsin Press)
[4] Staack D, Farouk B, Gutsol A and Fridman A 2005 Characterization of a dc atmospheric pressure normal glow discharge *Plasma Sources Sci. Technol.* **14** 700-711
[5] Staack D, Farouk B, Gutsol A and Fridman A 2008 DC normal glow discharges in atmospheric pressure atomic and molecular gases *Plasma Sources Sci. Technol.* **17** 025013
[6] Gangoli S, Gutsol A and Fridman A 2010 A non-equilibrium plasma source: magnetically stabilized gliding arc discharge: I. Design and diagnostics *Plasma Sources Sci. Technol.* **19** 065003
[7] Gangoli S, Gutsol A and Fridman A 2010 A non-equilibrium plasma source: magnetically stabilized gliding arc discharge: I. Electrical characterization *Plasma Sources Sci. Technol.* **19** 065004
[8] Fridman A, Nester S, Kennedy L A Saveliev A and Mutaf-Yardemci O 1999 Gliding arc gas discharge *Progress in Energy and Combustion Science* **25** 211-231
[9] Indarto A, Choi J-W, Lee H and Song H K 2005 Kinetic modeling of methane conversion using gliding arc *J. Nat. Gas Chem.* **14** 13-21
[10] Indarto A, Choi J-W, Lee H and Song H K 2006 Conversion of CO_2 by gliding arc plasma *Environ. Eng. Sci.* **23** 1033-1043
[11] Indarto A, Yang D R, Choi J-W, Lee H and Song H K 2007 Gliding arc processing of CO_2 conversion *J. Haz. Mat.* **23** 309-315
[12] Anders A 2009 *Cathodic Arcs: From Fractal Spots to Energetic Condensation* (New York: Springer)
[13] Benilov M S 2008 Understanding and modelling plasma-electrode interaction in high-pressure arc discharges: a review *J. Phys.* D: *Appl. Phys.* **41** 144001
[14] Jüttner B 2001 Cathode spots of electric arcs *J. Phys.* D: *Appl. Phys.* **34** R103-R123
[15] Mutaf-Yardimci O, Saveliev A V, Fridman A A and Kennedy L A 2000 Thermal and nonthermal regimes of gliding arc discharge in air flow *J. Appl. Phys.* **87** 16321641

[16] Kuznetsova I V, Kalashnikov N Y, Gutsol A F, Fridman A A, Kennedy L A 2002 Effect of "overshooting" in the transitional regimes of the low-current gliding arc discharge *J. Appl. Phys.* **92** 42314237

[17] Richard F, Cormier J M, Pellerin S and Chapelle J 1996 Physical study of a gliding arc discharge *J. Appl. Phys.* **79** 22452250

[18] Pellerin S, Richard F, Chapelle J, Cormier J-M, Musiol K 2000 Heat string model of bi-dimensional dc glidarc *J Phys* D: *Appl Phys* **33** 24072419

[19] Pellerin S, Cormier J-M, Richard F, Musiol K and Chapelle J 1999 Determination of the electrical parameters of a bi-dimensional d.c. glidarc *J Phys* D: *Appl Phys* **32** 891897

[20] Tu X, Gallon H J and Whitehead J C 2011 Electrical and optical diagnostics of atmospheric pressure argon gliding arc plasma jet, 30th ICPIG, August 28th September 2nd 2011, Belfast, Northern Ireland, UK, C10

[21] Tu X, Gallon H J and Whitehead J C 2011 Dinamic behavior of atmospheric argon gliding arc plasma, *IEEE Trans. Plasma Sci.* **39** 2900-2901

[22] BIAGI-v7.1 database, www.lxcat.laplace.univ-tlse.fr; Transcribed from SF Biagi's Fortran code MAGBOLTZ, Version 7.1, 2004. http://consult.cern.ch/writeup/magboltz

[23] Bartschat K, Zeman V 1999 Electron-impact excitation from the (3p54s) metastable states of argon *Phys. Rev.* **A59** 2552

[24] Hyman H A 1979 Electron-impact ionization cross section for excited states of the rare gases (Ne, Ar, Kr, Xe), cadmium, and mercury *Phys. Rev. A* **20** 855-859

[25] Raizer Yu P, Gas Discharge Physics, (Berlin: Springer) p 62

[26] Dyatko N A, Ionikh Y Z, Kochetov I V, Marinov D L, Meshchanov A V, Napartovich A P, Petrov F B and Starostin S A 2008 Experiemntal and theoretical study of the transition between diffuse and contracted forms of the glow discharge in argon *J Phys* D: *Appl Phys* **41** 055204

[27] Jonkers J, van de Sande M, Sola A, Gamero A, Rodero A and van der Mullen J 2003 *Plasma Sources Sci. Technol.* **12** 464-474

[28] Cunningham A J, O'Malley T F and Hobson R M 1981 On the role of vibrational excitation in dissociative recombination *J. Phys.* B: *At. Mol. Phys.* **14** 773-782

[29] Castaños-Martinez E, Kabouzi Y, Makasheva K and Moisan M 2004 Modeling of microwave-sustained plasmas at atmospheric pressure with application to discharge contraction *Phys. Rev.* E **70** 066405

[30] Kannari F, Suda A, Obara M and Fujioka T 1983 Theoretical simulation of electron-beam-excited xenon-chloride (XeCl) Laser *IEEE J. Quant. Electron.* **19** 1587-1600

[31] Hagelaar G J M and Pitchford L C 2005 Solving the Boltzmann equation to obtain electron transport coefficients and the rate coefficients for fluid models *Plasma Sources Sci. Technol.* **14** 722-733

[32] Lieberman M A, Lichtenberg A J *Principles of Plasma Discharges and Materials Processing*, (Hoboken: John Wiley & Sons) 2005 p 267

[33] Bultel A, Ootegem B, Bourdon A and Vervisch P 2002 Influence of Ar_2^+ in argon collisional-radiative model *Phys. Rev.* E **65** 046406

[34] Gregório J, Leprince P, Boisse-Laporteand C and Alves L L 2012 Self-consistent modelling of atmospheric micro-plasmas produced by a microwave source *Plasma Sources Sci. Technol.* **21** 015013

[35] Lam S K, Zheng C-E, Lo D, Dem'yanov A and Napartovich A P 2000 Kinetics of Ar_2^* in high-pressure pure argon *J. Phys.* D: *Appl. Phys.* **33** 242-251

[36] Mcdaniel E W and Mason E A 1973 *The mobility and diffusion of ions in gases* (Wiley)

[37] Ferreira C M, Loureiro J and Ricard A 1985 Populations in the metastable and the resonance levels of the argon and stepwise ionization effects in a low-pressure argon positive column *J. Appl. Phys.* **57** 82-90

[38] Hagelaar G J M, Fubiani G and Boeuf J-P 2011 Model of an inductively coupled negative ion source: I. General model description *Plasma Sources Sci. Technol.* **20** 015001

[39] Comsol Multiphysics 4.3a, Plasma module user's guide

[40] Jünter B, Puchkarev V F, Hantzsche E and Beilis I 1995 in *Hanbook of vacuum arc science and technology. Fundamentals and Applications* eds Boxman R, Sanders D M, Martin P M (Park Ridge, New Jersey: Noyes Publications) pp 158-174.

[41] Electron work function of the elements 2007 in *CRC Handbook of Chemistry and Physics* ed Lide D R (Taylor and Francis, Boca Raton, FL)

[42] Latham R V and Xu N S Electron pin-holes: the limiting defect for insulating high voltages by vacuum, a basis for new cold cathode electron sources 1991 *Vacuum* **42** 1173-1181

[43] Richard F, Cormier J M, Pellerin S and Chapelle J 1997 Gliding arcs fluctuations and arc root displacement *High Temp. Mater. Processes* **1** 239-248

[44] Pellerin S, Cormier J M, Musiol K, Pokrzywka B, Koulidiati J, Richard F and Chapelle J Spatial fluctuations of gliding arc 1998 *High Temp. Mater. Processes* **2** 49-68

[45] Delair L, Brisset J L and Chéron B G Spectral electrical and dynamical analysis of a 50 Hz air gliding arc 2001 *High Temp. Mater. Processes* **5** 381-403.

[46] Pellerin S, Martinie O, Cormier J M, Chapelle J and Lefaucheux P Backbreakdown phenomenon in low current discharge at atmospheric pressure in transversal flow 1999 *High Temp. Mater. Processes* **2** 167-180